

Dielectric Barrier Discharge-Induced Vortex Generation With Discharge-Actuated Boundary Layer Bleed

Seong-Kyun Im, Moon Soo Bak, Mark Godfrey Mungal, and Mark A. Cappelli

Abstract—The characteristics of vortices induced by spanwise forcing using a streamwise-oriented dielectric barrier discharge (DBD) vortex generator (VG) are investigated with and without a boundary layer bleed slot, the flow of which is also driven by a DBD actuator. The velocity fields of the induced flows are characterized by ensemble averaged particle image velocimetry. A stronger downward motion and proximity of the induced vortex to the forcing electrode and the wall are observed when the DBD VG is used in conjunction with a DBD-active bleed slot. The effect of varying the applied voltage and freestream velocity on the induced vortex is examined. Researches are carried out on the ability for this DBD VG to control the separation on an inclined flat-plate and diverging ramp. We find that the DBD VG, together with DBD-activated bleed slots, leads to more robust separation control in these adverse pressure gradient configurations.

Index Terms—Flow control, plasma application.

I. INTRODUCTION

VORTEX generators (VGs) have been studied for decades because of their practical use in separation control [1]. Separation control is important for pressure recovery in several fluid and aerodynamics applications. The idea of separation control using VGs was first introduced in [2] in late 1940s. By inducing streamwise (longitudinal) vortices, slow, and lower momentum fluid residing in the inner boundary layer is mixed with and displaced by higher momentum fluid drawn into the near surface from the freestream flow. Thus, the overall flow field has a higher propensity to overcome the adverse pressure gradient that would otherwise cause the flow to separate. Because of this behavior, vortex generation has been used to enhance lift and to reduce drag on various aircraft components (wing, engine, fuselage, and so on) [3], [4]. Typically, vane-type VGs of various sizes (down to the micrometer scale), angles, shapes, and array types have been studied and employed in practice [5]. Although there are vastly

different types of vane-type VGs concurrently in use, they all share similar designs and features. They generally consist of an array of plates or small airfoils that project from the aerodynamic body surface into the flow at an angle relative to the incoming freestream.

The induced vortex structures and interactions between vortex pairs have been studied in [6] and [7]. While VGs are very effective in separation control (especially during taking off and landing), their application comes at the expense of added drag because of the increased surface area. During certain times within an aircraft flight envelope (e.g., cruising mode) vortex generation is not needed and VGs can generate an undesirable wake and turbulence in addition to this increased drag. It is desirable to examine the methods in which vortices can be produced on demand with no moving parts and without introducing an additional drag. In this paper, we report on studies that employ a dielectric barrier discharge (DBD) actuator as a VG to avoid the drag induced by the physical protrusion into the flow of typical VGs.

A single-DBD actuator consists of exposed and dielectric-embedded electrodes driven by an alternating current (ac). Electrode pairs are oriented to induce a directional flow of neutral gas through collisions with the drifting ions [8]. DBD actuators for aerodynamic control applications have been studied for over a decade since they were first introduced in [9]. This directional flow has a suction-like effect that has proven to be useful in applications ranging from boundary layer transition delay [10], [11], boundary layer reattachment [12]–[14], and boundary layer control in subsonic [15] and supersonic [16] flow regimes. Several researchers have developed models and simulations of these DBD actuators [8], [17], [18]. The basic mechanism for how these discharge actuators work is fairly well understood. When operated in air, negative ions of oxygen play an important role as positive ions of nitrogen in transferring momentum to the neutral fluid resulting in a unidirectional force on both strokes of the ac cycle [19], [20].

The use of a single asymmetric DBD for spanwise forcing and vortex generation was recently studied in [21], which demonstrated successful actuation of a separated flow over a diverging ramp with surface-mounted DBD actuator arrays. These DBD VGs have a relatively high bandwidth response as they are electrically activated at tens of kilohertz frequencies. Because of this potential for reduced drag and high bandwidth control, DBD VGs have attracted much interest for a range of applications [22], [23].

Manuscript received April 30, 2013; revised August 5, 2013; accepted August 7, 2013. Date of publication August 22, 2013; date of current version December 9, 2013. This work was supported by the DOE-sponsored Predictive Science Academic Alliance Program. The work of M. S. Bak was provided through a Stanford Graduate Fellowship.

S.-K. Im, M. S. Bak, and M. A. Cappelli are with the Department of Mechanical Engineering, Stanford University, Stanford, CA 94305-3030 USA (e-mail: sim3@stanford.edu; moonsoo@stanford.edu; cap@stanford.edu).

M. G. Mungal is with the School of Engineering, Santa Clara University, Santa Clara, CA 95053 USA, and also with the Department of Mechanical Engineering, Stanford University, Stanford, CA 94305-3030 USA (e-mail: mungal@stanford.edu).

Color versions of one or more of the figures in this paper are available online at <http://ieeexplore.ieee.org>.

Digital Object Identifier 10.1109/TPS.2013.2278027

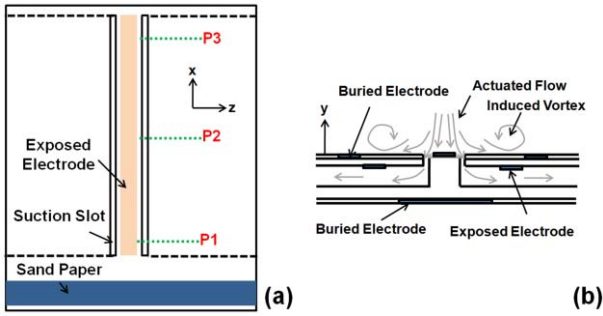


Fig. 1. Schematic diagram of DBD VG with bleed slot. (a) Top view. (b) Cross-sectional view.

As mentioned above, the mechanism of VG separation control is boundary layer mixing. When the generated vortex, however, lifts away from the wall, mixing is no longer effective. It is desirable then to keep vortices close to the surface for persisting mixing. In this paper, we investigate the additional removal of the low speed fluid that is displaced by the drawn-in higher speed fluid by introducing a bleed channel driven through an internal DBD actuation [24]. With this boundary layer bleed, it is significantly enhancing the separation control.

II. EXPERIMENTAL SETUP

The DBD configuration used here for vortex generation has been described in detail in [24]. It consists of an acrylic flat plate with an integrated bleed channel and several DBD actuator pairs. In this paper, we use this actuator to enhance vortex generation by adding boundary layer bleed. In this way, it is shown to be more robust than the case without active bleed. Fig. 1 (top- and cross-sectional views) shows the DBD device integrated into a 20° 130-mm wide and 230-mm long wedged flat plate. A symmetric DBD actuator pair is fabricated into the center of flat plate. The acrylic flat plate itself (5-mm thick) and Kapton tape (50- μm thick) are used as a dielectric material to isolate the embedded electrode for the symmetric DBD actuator pair. The exposed and embedded electrodes are 0.1-mm thick copper strips oriented parallel to the freestream flow. These electrodes, exposed and embedded, are 135 mm in length and 7-mm wide, and 135 mm in length and 50-mm wide, respectively. The freestream flow is referred to as the x -direction and the direction spanwise to the freestream flow is referred to as the z -direction. The direction normal to the flat plate is the y -direction. The center of the leading edge of the flat plate is assigned to be the origin of the coordinates, $(x, y, z) = (0, 0, 0)$. Both electrodes are placed along the center of the device 50 mm from the leading edge of the plate, $(x, y, z) = (50, 0, 0)$, and the exposed electrode is centered over the embedded electrode. The boundary layer is tripped by sand paper (130-mm wide and 20-mm long, 120 Grit) attached to the top surface of the flat plate 5-mm downstream ($x = 5$ mm) from the leading edge.

Two bleed slots of 1.5-mm width straddle the exposed electrode, 1 mm from either side of the electrode. These slots are connected to a 2-mm height inner channel that draws away the fluid from the bleed slot, eventually diverting these

fluids into the freestream at the side of the flat plate, as schematically shown in Fig. 1(b). Additional asymmetric DBD actuator pairs are integrated into the upper surface of the internal channels. The exposed and embedded electrodes of these pairs are located at $z = \pm 35$ and ± 42 mm from the center of the device, respectively. Both electrodes (exposed and embedded) are $d = 7$ -mm wide and $l = 115$ -mm long. Case acrylic (1.5-mm thick) and Kapton tape (50- μm thick) are used as the dielectric barrier for these internal actuators. In this device, the main symmetric electrode pair serves to induce a symmetric spanwise actuation, producing a downward fluid motion, as schematically shown in Fig. 1(b). This results in a displacement of the inner boundary layer by the higher speed fluid. A portion of the fluid in the inner boundary layer is diverted into the adjacent bleed slot by the actuation of the primary DBD pair and pushed laterally by the forcing from the asymmetric actuators within the internal channel. The fluid in the boundary layer that does not enter the bleed slot produces a spanwise directional (z -direction) motion on the top surface of the flat plate. This directional fluid motion interacts with freestream flow resulting in an induced vortex pair, as schematically shown in Fig. 1(b).

The primary symmetric DBD actuator pair and two secondary asymmetric DBD actuator pairs are powered by two independent ac power supplies. A Minipuls 6 power supply (GBS Elektronik GmbH) is used to energize the main pair. In this paper, a 13.0–15.5-kV (peak-to-peak) operating voltage and 15-kHz frequency are used for the primary symmetric DBD. The power consumed by the primary DBD actuator is ~ 13 –18 W, depending on the applied voltage. The two asymmetric actuators inside the bleed channels are powered by an Information Unlimited PVM 300 generator with a fixed driving voltage and frequency of 12 kV (peak-to-peak) and 25 kHz, respectively. The power consumption by these pairs is ~ 15 W. The consumed power by these electrodes is determined from the driving frequency and the integrated area under the characteristic charge (Q)—applied voltage (V) curve [25]. Typical maximum-induced speed by the primary DBD actuator was 1.5–2.0 m/s depending on actuation voltage. This speed was determined by particle image velocimetry (PIV) measurement in quiescence air.

This DBD VG model is tested in a $W = 300 \times H = 300$ -mm² cross-sectional area vertically operating wind tunnel that can generate up to 5.5 m/s in base flow ($Re_w = 1.04 \times 10^5$), as shown in Fig. 2. The model is placed at the center of the wind tunnel test section to minimize the influence from the wind tunnel wall (boundary layer and wall turbulence). In this paper, the freestream speed is varied from 2.0 to 5.5 m/s, with $< 0.3\%$ base turbulence intensity. This DBD VG device, enhanced by boundary layer DBD-induced bleed, is used to study its ability to control flow separation. Two cases were investigated. These are shown schematically in Fig. 3. The Case 1 [see Fig. 3(a)] is flow over the VG plate shown in Fig. 1, but inclined at an angle of 8° relative the freestream flow. The other [see Fig. 3(b)] is separation on a 25° diverging ramp added downstream of the DBD embedded flat plate with the VG plate parallel to the flow. This ramp has the same width as the VG plate and is

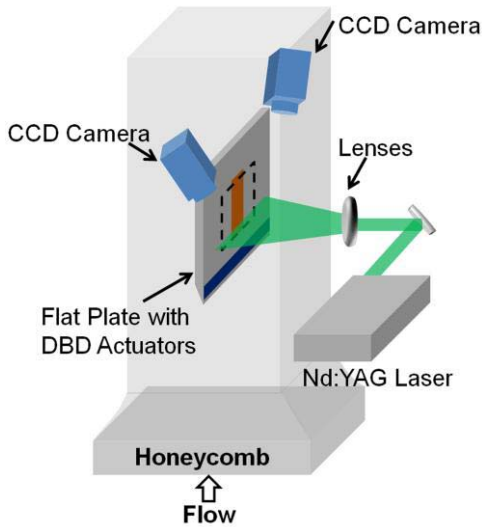


Fig. 2. Schematic diagram of the experimental setup.

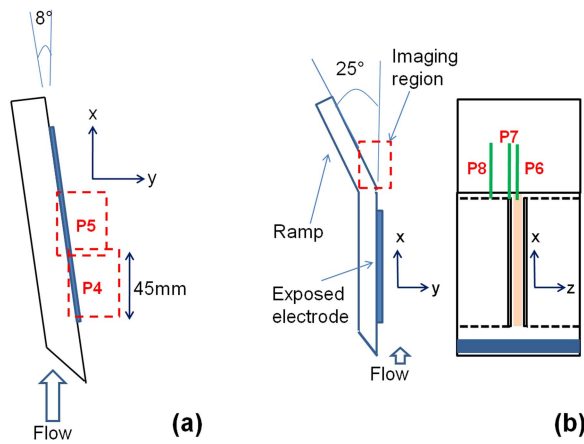


Fig. 3. Schematic diagram of separation study models. (a) Inclined flat plate. (b) Diverging ramp.

200 mm in length. A Nd:YAG laser (New wave, Gemini PIV, 100-mJ/pulse energy, 3 Hz, 532 nm) is shaped into a thin sheet using two cylindrical lenses and a convex spherical lens, and is directed into the test section for the PIV studies. For the PIV diagnostics, double exposure charge-coupled device cameras (La Vision, Imager intense) capture the scattered light from submicrometer size alumina particles. The velocity vector field is obtained from two instantaneous sequential images taken with a 50- μ s time delay. Laser shot timing and the triggering of the camera are synchronized by DaVis 7 software. PIV images are taken with three different flow conditions: (Case 1) flow without actuation, (Case 2) flow with DBD VG enhanced with boundary layer bleed (i.e., diverted flow induced by the DBD actuators within the bleed channel), and (Case 3) flow with DBD VG but with the bleed channels blocked. The two asymmetric channel actuators are not activated in Case 3, i.e., DBD VG acts like standard symmetric DBD VG. PIV images were processed by DaVis 7. Decreasing interrogation size with multipass calculation, two passes for 64 by 64 pixels and two passes for 32 by 32 pixels with 50% overlaps, was

selected for vector calculation. Eventually, PIV calculation returns the velocity vectors separated by ~ 0.75 mm each other. Every other vector is presented all of the following PIV velocity field results. PIV measurements are performed to investigate the flow induced by the DBD VG at three planes (P1 to P3, $x = 60, 110,$ and 160 mm), which are perpendicular to the freestream, as shown in Fig. 1(a), when the plate is oriented parallel to the freestream flow. The region captured in the P1 to P3 images span a distance $z = 3$ mm to $z = 33$ mm and $y = 30$ mm in height. Two (P4 and P5) and three (P6 to P8) more planes are used to record the PIV images for the separation control study on the 8° inclined DBD VG plate and on the 25° flap downstream of the DBD VG device, as shown in Fig. 3(a) and (b), respectively. The regions captured in the imaging plane for P4 and P5 are at the center plane of the plate ($z = 0$ mm) and span a 45 mm (in x -direction) by 30 mm (in y -direction) region of interest starting at $x = 50$ mm and 90 mm, respectively. P6 to P8 planes begin at $x = 230$ mm and span a 40 mm (in x -direction) by 30 mm (in y -direction) region of interest. P6 to P8 planes are located at $z = 0, -5,$ and -25 mm, respectively.

III. RESULT AND DISCUSSION

The boundary layer thickness at the upstream edge of the external forcing electrode determined by PIV measurements for 2.0, 3.8, and 5.5 m/s is $\delta = 5.5, 4.0,$ and 3.0 mm, respectively.

The induced streamwise vortices by DBD VG are shown in Fig. 4 for the case where the plate is oriented parallel to the flow. These images display the velocity fields for Cases 2 and 3 (activated DBD VG but with/without active boundary layer bleed, in Case 3, bleeding channel was blocked) of regions P1 to P3, obtained by ensemble averaging 250 stereo PIV image pairs. The direction of the freestream flow and coordinates in these images are shown. The two flow components (y -, z -direction) are shown by arrows whereas vorticity is represented by gray-scale contours. Fig. 4(a) and (b) are for conditions of 13.0-kV_{p-p} applied voltage at 2.0-m/s freestream flow. At these conditions, vortex formation is clearly apparent. The spanwise flow induced by DBD VG results in a localized circulation that grows in strength and size along the external flow direction. As this region of circulation grows, the vortex convects away from the exposed electrode and lifts away from the wall. This observation is consistent with the study in [21]. In the presence of the bleed slot [Fig. 4(a)], vortex formation and propagation appears to take on a slightly different characteristic, than that when the slot is blocked and internal DBDs are inactive [Fig. 4(b)]. A stronger downward and counter clockwise motion near the electrode is observed with active bleed. Thus, the vortex forms and resides closer to the electrode and the wall throughout its transit. The z -directional forcing by the DBD VG causes the vortex to migrate away from the electrode (z -direction). Results with a slightly higher driving voltage (15.5 kV_{p-p}) are shown in Fig. 4(c) and (d). They are qualitatively similar to those observed at the lower discharge voltage, with the exception that the vortex residence in the spanwise direction appears to

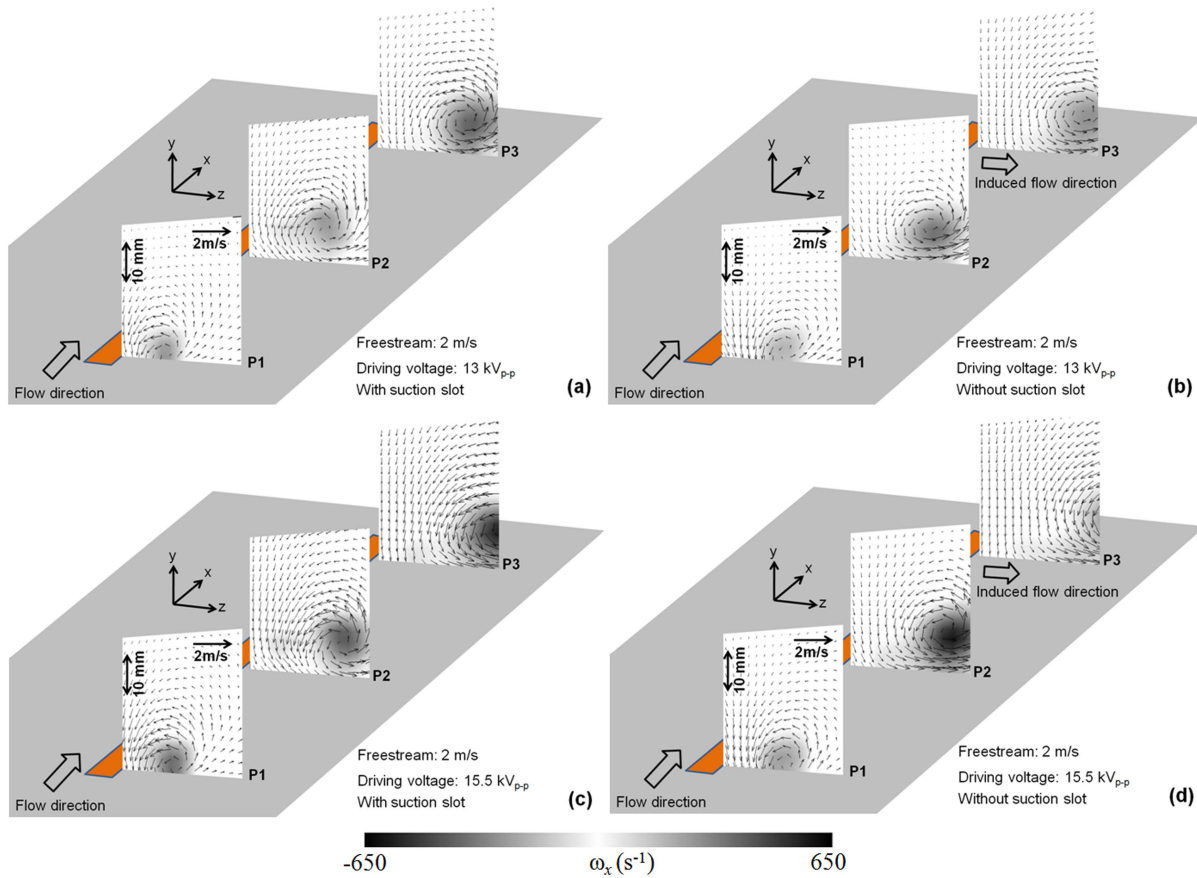


Fig. 4. Mean velocity fields at 2-m/s freestream speed with 13.0-kV_{p-p} driving voltage (a) Case 2 and (b) Case 3, with 15.5 kV_{p-p} (c) Case 2 and (d) Case 3.

be significantly shortened and the vortex strength is increased as a result of the increased spanwise forcing.

The effect of freestream speed on the induced flow is shown in Fig. 5(a)–(c). Here, freestream speeds are 2.0, 3.8, and 5.5 m/s, and the applied voltage to the primary DBD actuator pair is 15.5 kV_{p-p}. Flow fields including induced vortices by the DBD VG for the P1 and P3 imaging planes for Cases 2 (with an active bleed slot) and 3 (inactive bleed and blocked bleeding channel) flow conditions are acquired by ensemble averaging 250 stereo PIV image pairs. PIV results for Cases 2 and 3 are shown in the right and left-hand side of the main exposed electrode, respectively, to facilitate comparisons. The process and mechanism of the vortex formation remain the same as that observed in Fig. 4, but the characteristics of the vortices are different for each freestream speed case studied. As the speed increases, the downward motion in the P1 plane for Cases 2 and 3 flow conditions decreases. As shown in Fig. 5, the DBD VG enhanced with boundary layer bleed (right side) gives rise to induced vorticity that remains closer to the wall and to the electrode when compared with the DBD VG without bleed (left side), and the strength of the vortices for all speeds appear stronger than that with the blocked and inactive bleed slot. We observe that with an increasing speed, the lateral (z) displacement of the vortices is reduced for any axial (x) position in both Cases 2 and 3 flow conditions. This is due to a reduced residence time of the flow to actuation.

We also note, however, that the actuation power itself is affected by the change in flow speed. Visual observations of the discharge emission indicate that the active length of the discharge diminishes as the freestream speed increases. This is expected to result in a reduction in actuator effectiveness as previously reported in [26].

The spanwise (z -direction) and vertical (y -direction) positions of the induced vortices along the freestream flow direction (x -direction) are shown in Figs. 6 and 7. Zero values for x/d , y/l , and z/d are at the leading edge of the forcing electrode, at the surface of the wall, and the side edge of the forcing electrode. The location of vortex is defined by the center of the vortex core (where the speed is lowest) in the circulating region. The trajectories of the vortices, induced in Cases 2 and 3, with fixed applied voltage (13.0 kV_{p-p}) and various freestream flow speed, are shown in Fig. 6. In this figure, trajectories induced by DBD VG enhanced with boundary layer bleed (Case 2) and just DBD VG (Case 3), are shown as solid and dashed lines, respectively. Markers (red circles, black squares, and blue diamonds) represent a freestream speed of 2.0, 3.8, and 5.5 m/s, respectively. As expected, the vortex is initiated at a location slightly away from the forcing electrode and above from the surface, and migrating further away from the forcing electrode and lifting from the wall as the base flow is convected along streamwise direction. This principle applies to all vortices in Cases 2 and 3. It is, however,

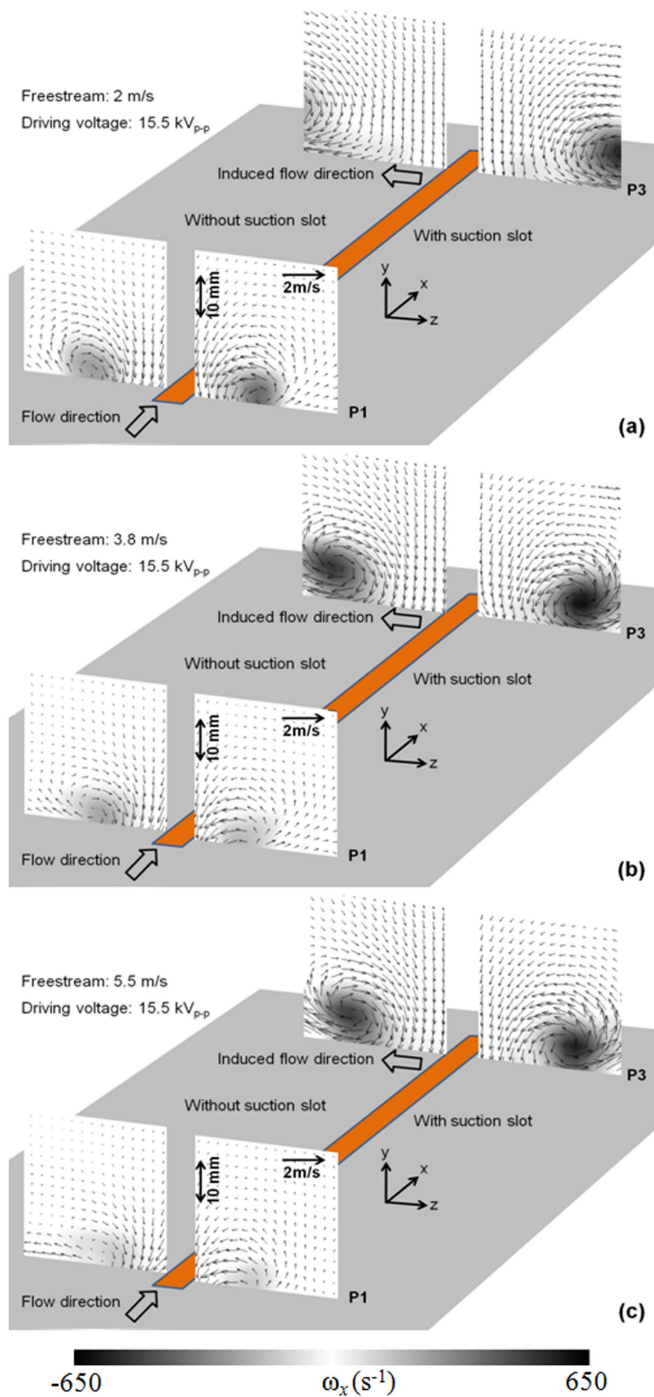


Fig. 5. Mean velocity fields at P1 and P3 PIV planes with 15.5 kV_{p-p} for Cases 2 and 3 with freestream speed at (a) 2.0, (b) 3.8, and (c) 5.5 m/s.

noteworthy that the initial location of generated vortex and the trajectory for Case 2 have different characteristics than those of Case 3. The initial vortex location and trajectory in Case 2 is closer to the forcing electrode and the surface than that of Case 3. It is also noteworthy that the trajectory in Case 2 is concave in shape as viewed from the forcing electrode (decreasing gradient in the z -direction), whereas that of Case 3 has a convex curvature (increasing gradient in the z -direction). We believe that this is mainly because of the downward motion to the activated bleed slot. As the freestream speed increases,

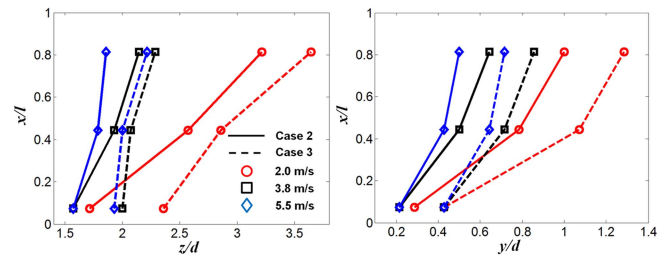


Fig. 6. Trajectory of the vortex induced in Case 2 (solid line) and Case 3 (dashed line) with 13.0-kV_{p-p} driving voltage at 2-m/s (circle), 3.8-m/s (square), and 5.5-m/s (diamond) freestream speed.

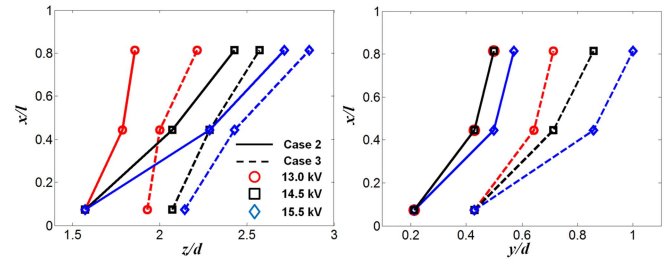


Fig. 7. Vortex trajectory for Case 2 (solid line) and Case 3 (dashed line) at 5.5-m/s freestream speed with (a) 13.0 kV_{p-p} (circle), (b) 14.5 kV_{p-p} (square), and (c) 15.5-kV_{p-p} (diamond) driving force.

the vortex trajectory moves closer to the forcing electrode and the wall surface. This is due to the decreased residence time to actuation and a possible reduction in actuation power.

A similar vortex trajectory characteristic is observed when the freestream speed is held constant (fixed vortex residence time) at 5.5 m/s and when the applied voltage to the external forcing electrode pair is varied, as observed in Fig. 7. In this figure, trajectories for Cases 2 and 3 are shown as solid and dashed lines, respectively. Markers (red circles, black squares, and blue diamonds) depict the vortex trajectory with 13.0, 14.5, and 15.5 kV_{p-p}, respectively. As expected, higher actuation power pushes and lifts the vortex further away from the forcing electrode and the wall surface, respectively. The vortex trajectory for Case 2 is much closer to the electrode and the wall surface than that of Case 3. The trajectory curvatures are similar in this case.

To help in explaining the differences observed between the characteristics of the induced vortex in Cases 2 and 3, we examine the spanwise (u_z) and the wall normal (u_y) velocity components measured at the P3 imaging plane 5 mm above the wall surface along the spanwise direction. First, we compare the velocity profile from the induced flow field with fixed applied voltage to the externally forcing electrode (15.5 kV_{p-p}) at two different freestream speeds. (3.8 and 5.5 m/s) Velocity components for Cases 2 and 3 are shown as the solid and dashed lines in Fig. 8. Blue squares and red circles represent a freestream speed of 3.8 and 5.5 m/s, respectively. A stronger downward motion is obtained near the external electrode in Case 2. Initially, we thought perhaps that the higher freestream speed leads to weaker downward motion because of a reduced actuation power. The strength of the induced downward motion, however, appears to be

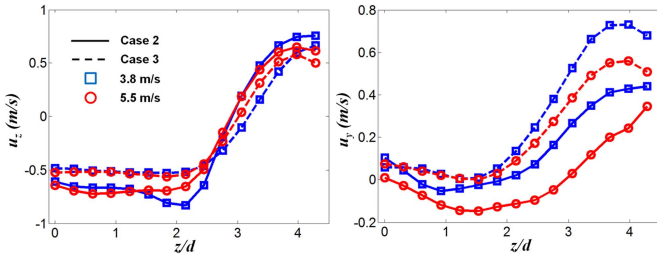


Fig. 8. Spanwise (u_z) and wall normal directional (u_y) velocity profile 5 mm above from the wall along the spanwise direction at P3 PIV imaging plane in Case 2 (solid line) and Case 3 (dashed line) with 15.5-kV_{p-p} driving force at 3.8- and 5.5-m/s freestream speed.

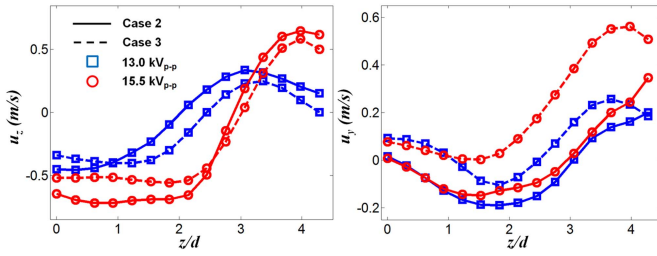


Fig. 9. Spanwise (u_z) and wall normal directional (u_y) velocity profile 5 mm above from the wall along the spanwise direction at P3 PIV imaging plane in Case 2 (solid line) and Case 3 (dashed line) at 5.5-m/s freestream speed with 13.0- and 15.5-kV_{p-p} driving force.

independent on the freestream speed. This suggests that there may be a stronger downward motion induced at a higher freestream speed that compensates for the weaker actuation. With the active bleed, there is a strong negative z -directional motion (toward forcing electrode) in Case 2, which we believe is responsible for the trajectory seen, with the vortex residing closer to the forcing electrode and the wall in Case 2.

Similar velocity profiles are observed for conditions of a fixed freestream speed (5.5 m/s) with two different applied voltages (13.0 and 15.5 kV_{p-p}), as shown in Fig. 9. As expected, the robustness in actuation decreases (as evidenced by the reduced downward motion) at lower applied voltage. However, there is always a stronger downward motion near the forcing electrode in Case 2 than in Case 3 for all applied voltages. Stronger downward and similar spanwise motions suggest that there would be more fluid diverted through the bleed slot at higher applied voltage.

The vortex strength that is induced by the DBD VG can be determined and compared by its circulation. The vortex circulation in this paper is calculated by integrating vorticity within a closed area, which contains > 75% of the peak vorticity. The calculated streamwise variation in the vortex circulation (normalized by the product of the local boundary layer thickness and freestream speed) is shown in Fig. 10. The circulation increases with increased applied voltage and decreasing freestream speed. The strength of vortex induced by the DBD VG with bleed and DBD VG without bleed (Cases 2 and 3, respectively) appears to be similar at identical flow conditions (applied voltage and freestream speed) and increases linearly along the streamwise direction. This shows that the DBD VG with bleed is able to create the same vortex

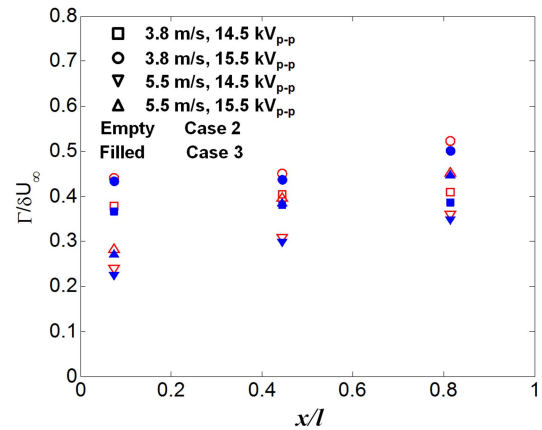


Fig. 10. Normalized circulation along the streamwise direction induced in Case 2 (empty) and Case 3 (filled).

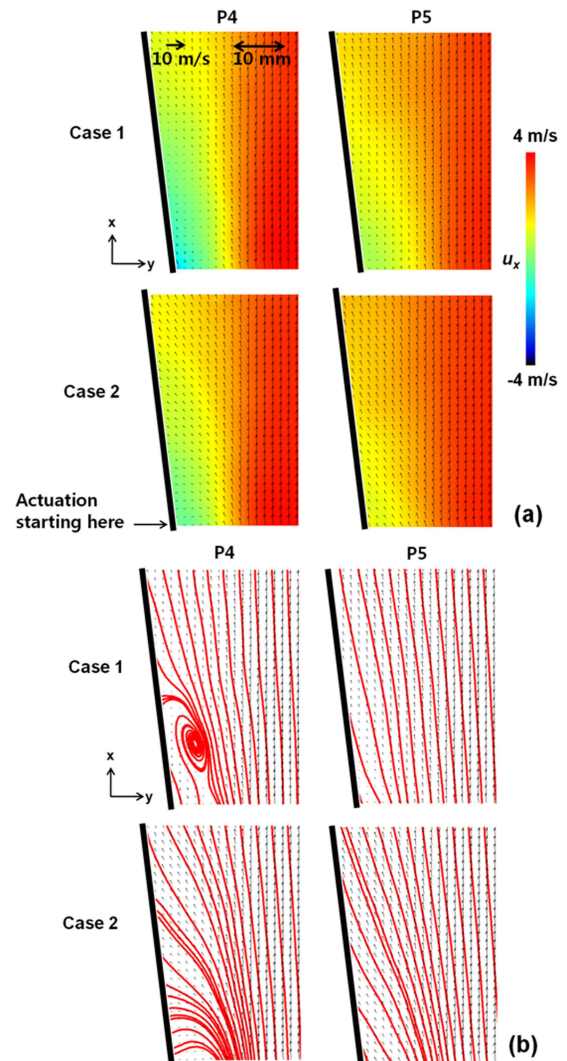


Fig. 11. (a) Mean velocity profile and (b) streamline for P4 and P5 PIV imaging planes with Cases 1 and 2 flow conditions at 3.8-m/s freestream speed.

strength as that of Case 3 and yet is able to enhance boundary layer mixing by modifying the vortex trajectory.

Separation control is investigated under two flow configurations. The first configuration is the DBD VG studied above,

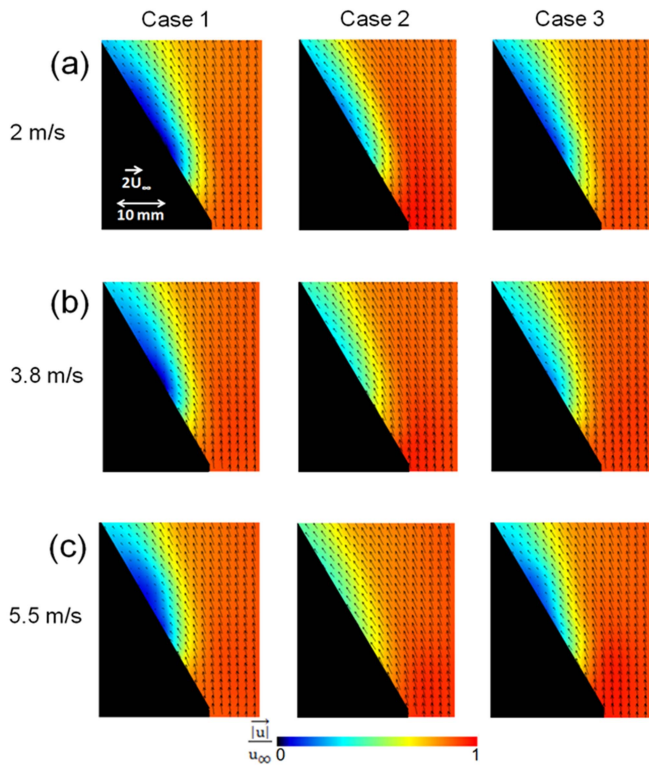


Fig. 12. Mean velocity profile for the P6 imaging plane with Cases 1–3 flow conditions at (a) 2-, (b) 3.8-, and (c) 5.5-m/s freestream speed.

with active bleed but tilted 8° relative to the freestream flow (i.e., separation on an inclined flat plate). The 2-D velocity fields and the streamlines, obtained by ensemble averaging 250 instantaneous PIV image pairs for imaging planes P4 and P5 [shown in Fig. 3(a)] with Case 1 (flow without any actuation) and Case 2 conditions at 3.8-m/s freestream flow are shown in Fig. 11. Arrows in this figure show the velocity components in the x - z plane whereas the color map [Fig. 11(a)] is just the x -component velocity. There is a region of recirculation in the P4 imaging plane for Case 1 flow condition confirming the presence of a separation bubble. The flow reattaches by the center of the P5 imaging plane. With the DBD VG with bleed actuation (Case 2), the flow reattaches further upstream than in Case 1 flow condition as observed from the streamlines shown in Fig. 11(b). The downward motion induced by the freestream exposed actuator is apparent in Case 2 flow condition at both the P4 and P5 planes. Considering that this DBD actuation begins near the upstream boundary of the P4 imaging plane, it appears then that there is an immediate influence of this actuation on separation in this configuration.

The second configuration for which separation control is investigated is the 25° diverging ramp positioned just downstream of the DBD VG device, as shown in Fig. 3(b). Fig. 12(a)–(c) shows the flow fields obtained by averaging 250 PIV image pairs for the P6 imaging plane with 15.5-kV_{p-p} driving voltage at 2.0, 3.8, and 5.5 m/s, respectively. All of the three flow conditions (Cases 1–3) are studied. The color map in this figure shows the velocity magnitude (normalized by the freestream speed). There is a clear separated region on the ramp surface without actuation (Case 1). The separated

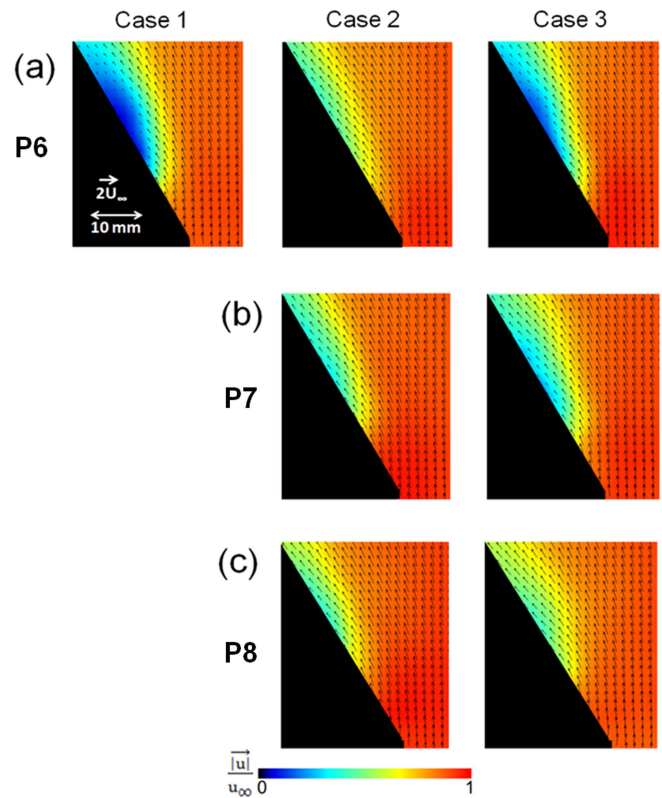


Fig. 13. Mean velocity profile for (a) P6, (b) P7, and (c) P8 imaging planes with Cases 1–3 flow conditions at 5.5-m/s freestream speed.

flow is weakened with DBD VG with bleed (Case 2). It is interesting to note that the effect is enhanced (in this plane) as the freestream speed is increased. We believe that this is because the vortex generated by the DBD places it closer to the region examined by the P6 plane as the freestream speed increases. The effect of actuation diminishes when the bleed slots are inactive (Case 3) indicating that the bleeding of the boundary layer has a major effect on the separation.

The mean flow field for the P6 to P8 imaging planes acquired by averaging 250 PIV image pairs with 15.5-kV_{p-p} driving voltage and 5.5-m/s freestream flow speed are shown in Fig. 13(a)–(c), respectively. The color map in this figure depicts the velocity magnitude (normalized by the freestream speed). The velocity field without actuation is shown on the top left corner of this figure. Flow separation is clearly observed on the P6 plane for Case 1. The mean velocity fields for the three different planes are essentially indistinguishable so we only show the flow field of Case 1 P6 case. An influence on the flow by DBD VG with bleed (Case 2) is observed in all planes. The effectiveness is, however, not nearly as strong in the case when the slot is blocked (Case 3). Case 3 effectiveness improves for planes P7 and P8 because of the arrival of the vortex generated by the DBD VG to these PIV planes, but the strength of actuation is not as strong as that in Case 2. The main reason of this is that the strength of the induced vortex and downward motion is less than that in Case 2 and the generated vortex is deflected farther from the wall, as observed from the detailed studies described above of the vortex generation and displacement.

IV. CONCLUSION

Experiments are carried out that characterize the vortex generation induced by a streamwise-aligned DBD designed to impart symmetric spanwise forcing and to generate streamwise vorticity. Bleed slots also driven by DBDs are used in conjunction with the DBD VG to enhance the performance of this VG on boundary layer mixing for separation control. Vortices induced by the DBD VG with the active bleed slots generate strong surface-directed motion in the vicinity of the external flow DBD electrode. Higher discharge voltages result in stronger-induced flow and increased vorticity. An increase in freestream speed is found to result in lower vortex strength and the trajectory of the vortex is much closer to the wall and exposed electrode. The reduction in the flow residence time in the discharge-active region is speculated to play a role in the recorded flow behavior. The downward motion induced by the DBD VG with bleed decreases as the freestream speed increases at the leading edge of DBD VG. A similar strength in the downward motion is, however, observed at the end of DBD VG. This is because of the movement of the higher momentum fluid toward the wall, compensating for weaker actuation.

The DBD VG with active bleed was examined for its ability to reattach the separated flows on an inclined (8° to the incoming flow) flat plate and on an aligned flat plate with a 25° trailing ramp. In both cases, the DBD VG with bleed increases the ability to reattach the separated boundary layer flows over a range of freestream velocities.

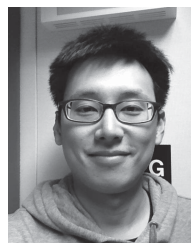
REFERENCES

- [1] D. Bushnell, "Longitudinal vortex control-techniques and applications," *Aeronaut J.*, vol. 96, pp. 293–312, Dec. 1992.
- [2] H. D. Taylor, "The elimination of diffuser separation by vortex generators," United Aircraft Corp., Moscow, Russia, Tech. Rep. R-4012-3, 1947.
- [3] M. B. Bragg and G. M. Gregorek, "Experimental study of airfoil performance with vortex generators," *J. Aircraft*, vol. 24, no. 5, pp. 305–309, May 1987.
- [4] W. Calarese, W. P. Crisler, and G. L. Gustafson, "Afterbody drag reduction by vortex generators," in *Proc. 36th AIAA Sci. Meeting*, Jan. 1995.
- [5] J. C. Lin, "Review of research on low-profile vortex generators to control boundary-layer separation," *Progr. Aerosp. Sci.*, vol. 38, nos. 4–5, pp. 389–420, May/Jul. 2002.
- [6] W. R. Pauley and J. K. Eaton, "Experimental study of the development of longitudinal vortex pairs embedded in a turbulent boundary layer," *AIAA J.*, vol. 26, pp. 816–823, Jul. 1998.
- [7] K. P. Angele and F. Grewe, "Instantaneous behavior of streamwise vortices for turbulent boundary layer separation control," *J. Fluids Eng.*, vol. 129, no. 2, pp. 226–235, Jun. 2006.
- [8] E. Moreau, "Airflow control by non-thermal plasma actuators," *J. Phys. D, Appl. Phys.*, vol. 40, no. 3, pp. 605–636, Feb. 2007.
- [9] J. R. Roth, D. M. Sherman, and S. P. Wilkinson, "Boundary layer flow control with a one atmosphere uniform glow discharge surface plasma," in *Proc. 36th AIAA Sci. Meeting Exhibit*, Jan. 1998.
- [10] S. Grundmann and C. Tropea, "Experimental transition delay using glow-discharge plasma actuators," *Exp. Fluids*, vol. 42, no. 4, pp. 653–657, Apr. 2007.
- [11] R. E. Hanson, P. Lavoie, A. N. Nagiub, and J. F. Morrison, "Transient growth instability cancellation by a plasma actuator array," *Exp. Fluids*, vol. 49, pp. 1339–1348, Dec. 2010.
- [12] M. L. Post and T. C. Corke, "Separation control on high angle of attack airfoil using plasma actuators," *AIAA J.*, vol. 42, pp. 2177–2184, Nov. 2004.
- [13] Y. Sung, W. Kim, M. G. Mungal, and M. A. Cappelli, "Aerodynamic modification of flow over bluff objects by plasma actuation," *Exp. Fluids*, vol. 41, no. 3, pp. 479–486, Sep. 2006.
- [14] H. Do, W. Kim, M. G. Mungal, and M. A. Cappelli, "Bluff body flow separation control using surface dielectric barrier discharges," in *Proc. 45th AIAA Aerosp. Sci. Meetings Exhibit*, Jan. 2007.
- [15] D. M. Schatzman and F. O. Thomas, "Turbulent boundary-layer separation control with single dielectric barrier discharge plasma actuators," *AIAA J.*, vol. 48, no. 8, pp. 1620–1634, Aug. 2010.
- [16] S. Im, H. Do, and M. A. Cappelli, "Dielectric barrier discharge control of a turbulent boundary layer in a supersonic flow," *Appl. Phys. Lett.*, vol. 97, no. 4, pp. 041503-1–041503-3, Jul. 2010.
- [17] A. V. Likhanski, M. N. Shneider, S. O. Macheret, and R. B. Miles, "Modeling of dielectric barrier discharge plasma actuator in air," *J. Appl. Phys.*, vol. 103, no. 5, pp. 053305-1–053305-13, Mar. 2008.
- [18] V. R. Soloviev and V. M. Krivtsov, "Surface barrier discharge modelling for aerodynamic applications," *J. Phys. D, Appl. Phys.*, vol. 42, no. 12, pp. 125208-1–125208-13, Jun. 2009.
- [19] A. W. Likhanskii, M. N. Shneider, S. O. Macheret, and R. B. Miles, "Modeling of interaction between weakly ionized near-surface plasmas and gas flow," in *Proc. 44th AIAA Aerosp. Sci. Meetings Exhibit*, Jan. 2006.
- [20] H. Do, W. Kim, M. A. Cappelli, and M. G. Mungal, "Cross-talk in multiple dielectric barrier discharge actuators," *Appl. Phys. Lett.*, vol. 92, no. 7, pp. 071504-1–071504-3, Feb. 2008.
- [21] T. N. Jukes and K.-S. Choi, "Dielectric-barrier-discharge vortex generators: Characterisation and optimisation for flow separation control," *Exp. Fluids*, vol. 52, no. 2, pp. 329–345, Feb. 2012.
- [22] Y. Okita, T. Jukes, K.-S. Choi, and K. Nakamura, "Flow reattachment over an airfoil using surface plasma actuator," in *Proc. 4th AIAA Flow Control Conf.*, Jun. 2008.
- [23] S. Grundmann, E. L. Sayles, and J. K. Eaton, "Sensitivity of an asymmetric 3D diffuser to vortex-generator induced inlet condition perturbations," *Exp. Fluids*, vol. 52, no. 1, pp. 11–21, Jan. 2012.
- [24] S. Im and M. A. Cappelli, "Dielectric barrier discharge induced boundary layer suction," *Appl. Phys. Lett.*, vol. 100, no. 26, pp. 264103-1–264103-4, Jun. 2012.
- [25] T. C. Manley, "The electric characteristics of the ozonator discharge," *J. Electrochem. Soc.*, vol. 84, no. 1, pp. 83–96, Jul. 1943.
- [26] C. A. Borghi, M. R. Carraro, A. Cristofolini, and G. Neretti, "Electrohydrodynamic interaction induced by a dielectric barrier discharge," *J. Appl. Phys.*, vol. 103, no. 6, pp. 063304-1–063304-11, Mar. 2008.



Seong-Kyun Im received the B.S. degree in mechanical and aerospace engineering from Seoul National University, Seoul, Korea, in 2007, and the M.S. and Ph.D. degrees in mechanical engineering from Stanford University, Stanford, CA, USA, in 2009 and 2013.

He is currently a Post-Doctoral Researcher with the Stanford Plasma Physics Laboratory, Department of Mechanical Engineering, Stanford University. His current research interests include aerodynamic flow control of subsonic/supersonic flow, compressible flow, plasma-assisted combustion, and supersonic combustion.



Moon Soo Bak received the B.S. degree in mechanical and aerospace engineering from Seoul National University, Seoul, Korea, in 2007, and the M.S. degree in mechanical engineering from Stanford University, Stanford, CA, USA, in 2010, where he is currently pursuing the Ph.D. degree with the Department of Mechanical Engineering.

He is a Research Assistant with the Stanford Plasma Physics Laboratory, Stanford University. His current research interests include combustion, fluid dynamics, and plasmas, plasma-assisted combustion, and atmospheric pressure plasmas.

Mr. Bak is a recipient of Stanford Graduate Fellowship.



Mark Godfrey Mungal was born in Trinidad, West Indies. He received the B.A.Sc. (Hons.) degree in engineering science from the University of Toronto, Toronto, ON, Canada, in 1975, and the M.S. and Ph.D. degrees in aeronautics from the California Institute of Technology, Pasadena, CA, USA, in 1977 and 1983, respectively.

He is currently the Dean of the School of Engineering, Santa Clara University, Santa Clara, CA, USA, and a Professor Emeritus with the Department of Mechanical Engineering, Stanford University, Stanford, CA, USA.

Dr. Mungal is a fellow of the American Physical Society and the American Society of Mechanical Engineers, an Associate Fellow of the American Institute of Aeronautics and Astronautics, and a member of the American Society of Engineering Education and the Combustion Institute.



Mark A. Cappelli received the B.A.Sc. degree in physics from McGill University, Montreal, QC, Canada, in 1980, and the M.A.Sc. and Ph.D. degrees in aerospace science and engineering from the University of Toronto, Toronto, ON, Canada, in 1983 and 1987, respectively.

He is currently a Professor with the Department of Mechanical Engineering, Stanford University, Stanford, CA, USA. His current research interests include plasmas and gas discharges as they apply to aerodynamic and space propulsion, combustion,

material processing, and biological processes.